Jamming transition and emergence of fracturing in wet granular media

by

Yue Meng

Submitted to the Department of Civil and Environmental Engineering
in partial fulfillment of the requirements for the degree of

Master of Science in Civil and Environmental Engineering

at the

MASSACHUSETTS INSTITUTE OF TECHNOLOGY

September 2020

Author .....
Department of Civil and Environmental Engineering
Aug 17, 2020

Certified by .....
Ruben Juanes
Professor of Civil and Environmental Engineering
Thesis Supervisor

Accepted by .....
Colette L. Heald
Professor of Civil and Environmental Engineering
Chair, Graduate Program Committee

Jamming transition and emergence of fracturing in wet granular media

by

Yue Meng

Submitted to the Department of Civil and Environmental Engineering
on Aug 17, 2020, in partial fulfillment of the
requirements for the degree of
Master of Science in Civil and Environmental Engineering

Abstract

The interplay between multiphase flow in a granular medium and the displacement of the grain particles generates a wide range of patterns, including fractures, desiccation cracks, and labyrinth structures. There are several controlling parameters behind the morphodynamics that govern the transition between different regimes. A modified capillary number characterizes the crossover from capillary fingering to viscous fingering, and a transition from fingering to fracturing can be achieved either by decreasing frictional resistance. The balance between frictional, viscous, and capillary forces has been studied in experiments and simulations, and has helped understanding the underlying mechanisms for a wide range of phenomena, including fractures in drying colloidal suspensions, and methane migration in lake sediments.

In this thesis we study fluid-induced deformation of granular media, and the fundamental role of capillarity and wettability on the emergence of fracture patterns. We develop a hydromechanical computational model, coupling a "moving capacitor" dynamic network model of two-phase flow at the pore scale with a discrete element model of grain mechanics. We simulate the slow injection of a less viscous fluid into a frictional granular pack initially saturated with a more viscous, immiscible fluid. We study the impact of wettability and initial packing density, and find four different regimes of the fluid invasion: cavity expansion and fracturing, frictional fingers, capillary invasion, and capillary compaction. We explain fracture initiation as emerging from a jamming transition, and synthesize the system's behavior in the form of a novel phase diagram of jamming for wet granular media.

Thesis Supervisor: Ruben Juanes
Title: Professor of Civil and Environmental Engineering

Acknowledgments

I would like to express my deepest gratitude to my research advisor, Ruben Juanes, for your encouragement, inspiring teaching, and patience. Your empathy and support helped me through difficult time, and grew much stronger;

To my dearest collaborator and mentor Bauyrzhan Primkulov, I am deeply grateful for your generous sharing of knowledge, patience and friendship. Through our daily interactions and deep conversations, I am inspired and transformed to a better person;

Juanes Research Group is my second family, that I always feel cared and supported here. I am deeply grateful to all my friends here, for your accompanies, supports, and all the intellectual or insightful discussions we have;

and, last but not least, to my parents Yueying Yang, Xiangwen Meng, and my sister Huan Meng. You always put my health and happiness as the priority, and love me with full respect, trust, and support. You make me vulnerable and strong at the same time, which enriches me in a precious way. My love for you will never fade with time, or distance.

THIS PAGE INTENTIONALLY LEFT BLANK

Contents

1 Introduction **13**

2 A fully-coupled model of two-phase flow and grain mechanics **17**

2.1 "Moving capacitor" dynamic network model of two-phase flow 17

2.2 Coupling of flow and grain mechanics 18

2.3 Model set-up 20

2.4 Sample preparation 21

3 Pattern formation and invasion dynamics **23**

3.1 Evolution of interface morphology during fluid invasion 23

3.2 Particle displacement field at breakthrough 24

3.3 Invasion events analysis 25

3.4 Signals of injection pressure and packing density 25

4 Mechanism behind emergence of fracturing: jamming transition **33**

4.1 Jamming transition analysis from classic metrics 34

4.2 Microscopic evidence for jamming transition: evolution of the contact force network 35

4.3 Phase diagram of jamming for wet granular media 36

4.4 Influence of grain properties on the jamming phase diagram 37

5 Conclusion **41**

THIS PAGE INTENTIONALLY LEFT BLANK

List of Figures

1-1 Visual phase diagram of fluid invasion patterns of a low viscosity liquid (light gray) into a glass-bead pack initially saturated with a high-viscosity liquid (dark), as a function of the static advancing contact angle θ and the modified capillary number Ca^*, for a confinement weight resting on top of the lid of $W = 15$ N and viscosity contrast between the fluids $M =\approx 350$ Adapted from Trojer et al. [1]. 15

2-1 Interface morphology and pore pressure field at breakthrough for initial packing fraction $\phi_0 = 0.77$ and different wetting conditions: (a) $\theta = 140°$, (b) $\theta = 65°$, (c) $\theta = 46°$. Bottom: zoomed-in view of the particles near the interface, where red arrows indicate the resultant of pore pressure forces acting on each particle. Adapted from Meng et al. [2]. 22

2-2 Jamming transition analysis for $\phi_0 = 0.77$, $\theta = 140°$. (a)-(e): Interface morphology at the jamming transition (black line) compared with that at breakthrough (red line) for five initial granular packs generated with different seed numbers; (f) Time evolution of injection pressure P_{inj}; and (g) Mean particle stress P as a function of packing density ϕ in the compacting granular layer for all five granular packs. Adapted from Meng et al. [2]. 22

3-1 Visual phase diagram of the invading fluid morphology at breakthrough corresponding to different substrate wettabilities (contact angle θ) and initial packing densities ϕ_0. We identify four distinct morphological regimes: (I) cavity expansion and fracturing, (II) frictional fingers, (III) capillary invasion, and (IV) capillary compaction. Adapted from Meng et al. [2]. 27

3-2 Evolution of interface morphology at $t_d(= t/t_{\text{breakthrough}}) = 0.2, 0.5, 1.0$. The insets show the capillary entry pressure (P_{cap}) for every throat at the fluid-fluid interface (black crosses) and the injection pressure at that moment (red line). (a) Cavity expansion and fracturing (regime I), $\phi_0 = 0.77, \theta = 140°$. (b) Frictional fingers (regime II), $\phi_0 = 0.77, \theta = 65°$. (c) Capillary invasion (regime III), $\phi_0 = 0.84, \theta = 46°$. (d) Capillary compaction (regime IV), $\phi_0 = 0.77, \theta = 46°$. Adapted from Meng et al. [2]. 28

3-3 Comparison of total particle displacement fields that develop under different wettability conditions. 29

3-4 Temporal profiles of invasion events happened throughout the process (red, blue, green cross represents burst, touch, overlap event separately). The vertical axis for the left, and right profile shows the injection pressure when an event happens, and the angle (θ) formed by the particle where the event happens and its two neighboring particles. The profiles for three contact angles are shown here: $(a)\theta = 65°.(b)\theta = 75°.(c)\theta = 120°$. 30

3-5 Time evolution of (a) injection pressure P_{inj}, and (b) packing density ϕ, for simulations with initial packing density $\phi_0 = 0.77$, and $\theta = 75°, 90°, 120°, 140°$. The crosses denote the jamming transition for each case. Adapted from Meng et al. [2]. 31

4-1 Jamming transition analysis for $\phi_0 = 0.77$, $\theta = 75°, 90°, 120°, 140°$. (a)-(c) Average maximum shear stress ($\tau_{\max}$), mean particle stress (P), and mean contact number (Z) as a function of packing density ϕ in the compacting granular layer. (a) inset: determination of the critical packing fraction at jamming. (b),(c) insets: $P - P_c$, $Z - Z_c$ as a function of $\phi - \phi_c$, exhibiting power-law trends; (d) Interface morphology at the jamming transition [identified from (a)] for $\theta = 75°, 90°, 120°, 140°$ (black line), compared with that at breakthrough (red line). The comparison confirms that the jamming transition determines the onset of fracturing. Adapted from Meng et al. [2]. . 38

4-2 Evolution of the contact-force network for $\phi_0 = 0.77$, $\theta = 140°$, at (a) $t_d = 0.2$, (b) $t_d = 0.4$, (c) $t_d = 0.6$ (jamming transition), (d) $t_d = 0.8$, and (e) $t_d = 1.0$. The thickness of the blue line is proportional to the magnitude of the interparticle force. Adapted from Meng et al. [2]. 38

4-3 Phase diagram of jamming for wet granular media when capillary forces dominate. Shown are the trajectories of the system in $(P^*_{\text{inj}}, 1/\phi)$-space for all the simulated cases of Fig. 3-1, ranging in contact angle θ from 140° (drainage) to 46° (imbibition), and ranging in initial packing density ϕ_0 from 0.68 (loose pack) to 0.84 (dense pack). Note the different scale of the horizontal axis for positive and negative injection pressures. For all four regimes of fluid invasion and grain deformation, the proposed diagram uniquely separates the system's unjammed state (blue) from its jammed state (gray), independently of θ and ϕ_0. In particular, this explains the onset of fracturing in capillary-dominated fluid-driven injection into granular packs (red symbols). Adapted from Meng et al. [2]. 39

4-4 Influence of grain properties on the jamming phase diagram for wet granular media when capillary forces dominate. (a) Coefficient of friction taking values $\mu = 0.1$, 0.3 and 0.5, (b) Shear modulus taking values $G = 25$, 50 and 100 MPa. Adapted from Meng et al. [2]. 40

THIS PAGE INTENTIONALLY LEFT BLANK

Chapter 1

Introduction

Immiscible fluid-fluid displacement in porous media is important in many natural and industrial processes, including the displacement of air by water during rainfall infiltration [3], storage of carbon dioxide in deep saline aquifers [4], contaminant soil remediation [5], enhanced oil recovery [6], and design of microfluidic devices [7]. While fluid-fluid displacement in rigid porous media has been studied in depth, fundamental gaps remain in our understanding of the interplay between multiphase flow in a granular medium and the displacement of the grain particles [8, 9]. This interplay can lead to a wide range of patterns, including fractures [10, 11, 12, 13, 14, 15, 16], desiccation cracks [17, 18], labyrinth structures [19], and granular and frictional fingers [20, 21, 22, 23]. There are several controlling parameters behind the morphodynamics that govern the transition between the different regimes. A modified capillary number, Ca^*, characterizes the crossover from capillary fingering to viscous fingering [24], and a transition from fingering to fracturing can be achieved either by decreasing frictional resistance [24], or setting the outer boundary as free [25]. The balance between frictional, viscous, and capillary forces has been studied in experiments [24, 19, 23] and simulations [26, 12], and has helped understand the underlying mechanisms for a wide range of phenomena, including venting dynamics of an immersed granular layer [27, 28, 29], fractures in drying colloidal suspensions [10, 14], and methane migration in lake sediments [30, 31, 32, 33].

As one of the factors that influences multiphase flow in porous media, wettability (the relative affinity of the substrate to each of the fluids, and measured by the contact angle θ) has been studied for decades. While much is now known about the role of wettability on

multiphase displacements in porous media [34, 35, 36, 37, 38, 39, 40, 41, 42, 43, 44, 45, 46, 47, 48, 49], fundamental gaps remain in the context of grain-scale mechanisms and their macroscale consequences. In a recent experimental set-up [1], a low-viscosity fluid is injected into a circular Hele-Shaw cell filled with a dense glass-bead pack that is saturated with a more viscous, immiscible fluid. By carefully tailoring the wetting condition of the fluid pair, the authors aim to explore the impact of wetting on fracturing of granular media. The key result is a visual phase diagram of fluid invasion and fracturing patterns as a function of capillary number and contact angle, as shown in Figure 1-1. The diagram demonstrates that the wetting properties exert a significant, non-monotonic impact on fracture morphology: highly ramified, disconnected, and ephemeral fracturing in drainage (Fig. 1-1, left); rigorous, hierarchical and persistent fracturing in weak imbibition (Fig. 1-1, middle); no fracturing in strong imbibition (Fig. 1-1, right). The physical mechanism responsible for the striking differences in the fracture morphology is a transition in the pore-scale fluid displacement from pore-invasion in drainage, to corner flow in imbibition.

These experimental results indicate that wetting condition plays a fundamental role in fracturing of porous media, even at high capillary numbers when viscous forces dominate. The conclusion is very inspiring and provokes modeling work that explores the interactions of fluid and grain mechanics at the pore-scale under the effect of wettability. Given the importance of capillarity on fracture of granular packs [12, 26, 23, 24, 16], here we focus on the impact of wetting properties on the emergence of such fracture patterns. We also adopt packing density as a control parameter, since it can lead to a transition from Saffman–Taylor instability to dendritic (or ramified) fingering patterns [50], or from frictional fingering to stick-slip bubbles [23].

In this thesis, we uncover four fluid-invasion morphological regimes under different initial packing densities and substrate wettabilities: cavity expansion and fracturing, frictional fingers, capillary invasion, and capillary compaction. To rationalize these simulation outputs, we propose to analyze the evolution of the system as one approaching a jamming transition, which provides new insights that allow us to map the wealth of behavior onto a novel phase diagram of jamming for wet granular media.

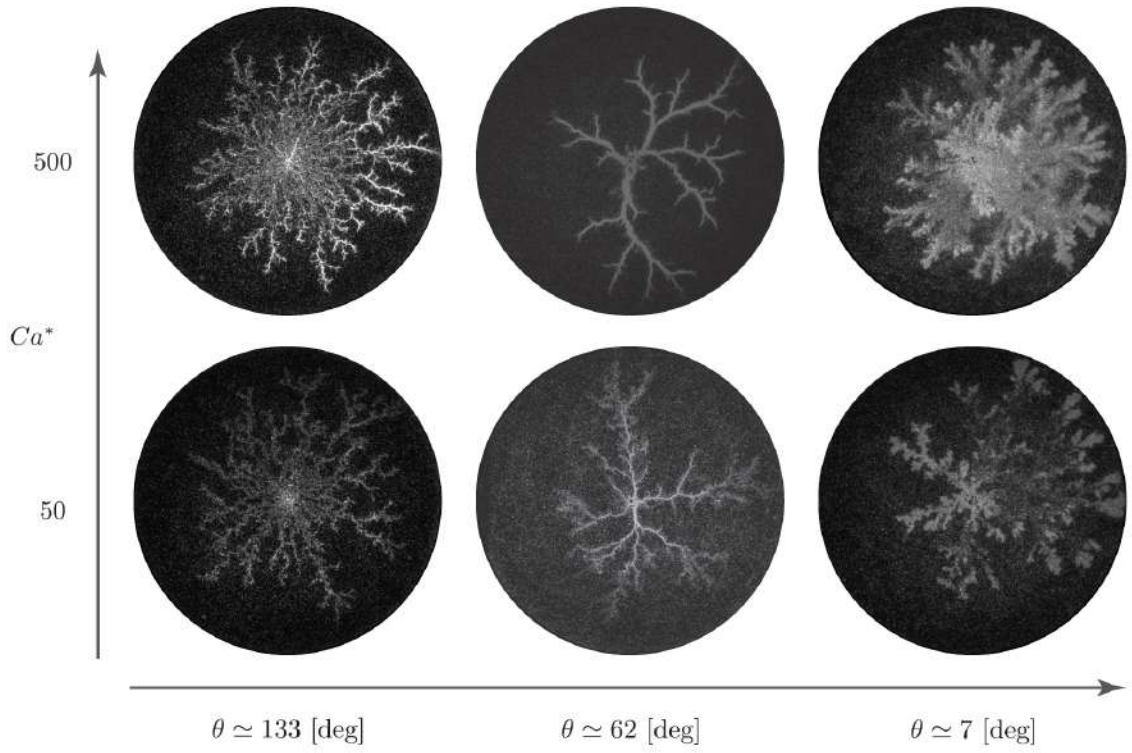

Figure 1-1: Visual phase diagram of fluid invasion patterns of a low viscosity liquid (light gray) into a glass-bead pack initially saturated with a high-viscosity liquid (dark), as a function of the static advancing contact angle θ and the modified capillary number Ca^*, for a confinement weight resting on top of the lid of $W = 15$ N and viscosity contrast between the fluids $M =\approx 350$ Adapted from Trojer et al. [1].

THIS PAGE INTENTIONALLY LEFT BLANK

Chapter 2

A fully-coupled model of two-phase flow and grain mechanics

2.1 "Moving capacitor" dynamic network model of two-phase flow

We model the fluid-fluid displacement with a dynamic pore network framework [46]. We approximate the pore geometry with a network of nodes and edges and take advantage of the analogy between the pore-scale fluid-fluid displacement and an electric circuit. Three key physical mechanisms make up the core of the model: (i) wettability effects, (ii) viscous forces, and (iii) capillary forces. Wettability effects are captured through the pore-scale invasion mechanisms outlined by Cieplak and Robbins [37, 38], and the invading front transits from invasion-percolation to cooperative filling as θ changes from 140° to 46° Primkulov et al. [45]. The dynamic effects are captured through the analog electric circuit, where resistors are responsible for viscous pressure drops, and batteries and capacitors are responsible for capillary pressure drops. The fluid-fluid interface is represented as a moving capacitor: as the local fluid interface advances, the Laplace pressure increases until it encounters a "burst" (equivalent to a Haines jump), "touch" (invading fluid touches the nearest particle), or "overlap" event (neighboring interfaces coalesce) [38, 37]. Given these approximations, the problem can be reduced to a system of linear equations at every time step [46].

If one utilizes the incidence matrix A to store the network topology, then the Poiseuille-type flow through the network and the conservation of mass at the nodes yield the following

system of equations:

$$\begin{cases} q = C(b - Ap), \\ A^\top q = f, \end{cases} \tag{2.1}$$

where p stands for pore pressure, b the pressure change across batteries, q the flow rate, C the throat conductance, and f the source of current at the nodes. The pressure drop across a capacitor at time t is $\Phi(t)\Delta p_{\text{crit}}$, where $\Phi(t) = \frac{V(t)}{V_{\text{tot}}}$ is the volume fraction of the invading fluid in a tube. The critical Laplace pressure drop Δp_{crit} is taken to be the smallest of the local "burst", "touch", and "overlap" event pressures [45]. Then, taking into account the direction of the edges ($d(t) = 1$ or -1), the pressure drop across the network in two-phase flow model is $e = b - Ap - d(t)\Phi(t)\Delta p_{\text{crit}}$. Therefore, the governing equations for two-phase flow is [46]:

$$\begin{bmatrix} C^{-1}(t) & A \\ A^\top & 0 \end{bmatrix} \begin{bmatrix} q(t) \\ p(t) \end{bmatrix} = \begin{bmatrix} b - d(t)\Phi(t)\Delta p_{\text{crit}} \\ f \end{bmatrix}, \tag{2.2}$$

where the elements of the conductance matrix $C(t)$ are calculated as $c_i(t) = \frac{\pi r^4}{8\eta_{\text{eff}}(t)L}$, assuming fully developed Hagen-Poiseuille flow through a capillary tube of radius r and length L. The effective viscosity at the invading fluid front is taken as $\eta_{\text{eff}}(t) = \Phi(t)\eta_{\text{inv}} + (1 - \Phi(t))\eta_{\text{def}}$.

2.2 Coupling of flow and grain mechanics

To capture particle motion, we couple the dynamic flow network model with a discrete element model (DEM), PFC2D® [**?** 51]. Hydromechanical two-way coupling is achieved from three perspectives: (1) the fluid pressures calculated from the moving-capacitor flow model exert forces on particles, and lead to particle rearrangement and deformation; (2) particle movements change the geometric configuration of the granular pack, which in turn changes the pore network topology and throat conductances and capillary entry pressures; and (3) expansion of the central cavity around the injection port "consumes" injected fluid, which decreases the flow of fluid permeating through the granular pack. The net force on each particle has two components: (1) contact forces calculated from the Hertz-Mindlin contact model [51], and (2) pore-pressure forces. Figure 2-1 shows the pore-pressure field at breakthrough for a low injection rate (Ca*=0.5), initial packing fraction $\phi_0 = 0.77$, and different wetting conditions $\theta = 140°$, $65°$, and $46°$. The differences in pressure field and the resultant pore-pressure force acting on the particles at the interface illustrate clearly

the impact of wettability. At $\theta = 140°$, the resultant pore-pressure forces point outwards, with a characteristic magnitude of ~ 0.2 N. At $\theta = 65°$, the resultant forces also point outwards, but they are an order of magnitude smaller, ~ 0.02 N. At $\theta = 46°$, in contrast, the resultant pore-pressure forces point inwards, and they are directly responsible for capillary compaction. During the injection process, the water–oil interface advances in a pore-by-pore manner, with particles immersed either in water or oil. Therefore, fluid distribution in our granular system cannot be described in terms of pore-scale morphologies used for wet granular media at low liquid saturations [52]. For our fully-saturated granular pack, capillary interactions do not elicit attractive forces brought by capillary bridges [53, 54] but, rather, by the pore-pressure forces acting on the particles, which depend strongly on the system's wettability.

To achieve an effective hydromechanical two-way coupling, the pore volume change should feed back into the pressure calculations [12, 22, 55]. For computational efficiency, we implement such coupling for the cavity volume, a region surrounded by interface particles [22]. Here, we keep track of the cavity volume evolution and set $Q_{\text{inj}} = Q_{\text{int}} + \frac{\Delta V_{\text{cav}}}{\Delta t_{\text{fluid}}}$, where Q_{inj} is the injection flowrate, Q_{int} the flowrate at the interfaces, ΔV_{cav} the cavity expansion volume, and Δt_{fluid} the fluid time step. As a result, the injected fluid is consumed either by filling interface throats, or by filling the expanded cavity volume during that injection period. We set the constant injection flowrate Q_{inj} corresponding to the prescribed Ca^*.

We assume the flow to be incompressible, and thus the flow model outputs the steady-state pressure profile after the relaxation of viscous gradients. As a result, the model works best for slow displacement in deformable granular packs. In this regime viscous pressure gradients have time to relax between front movements and capillary effects govern the displacement [56], which prompts us to set $\text{Ca}^* = 0.5$. To guarantee that the capillary pressure drop outweighs the viscous pressure drop, we found that a smaller Ca^* is needed when out-of-plane instead of in-plane Laplace pressure dominates. When the negative out-of-plane and the positive in-plane Laplace pressures are comparable in magnitude ($\theta = 46°, 55°$ here), we take $\text{Ca}^* = 0.0005$. Although this brings additional computational cost, we gain two significant advantages: (1) the injection pressure signal only reflects the minimal capillary pressure along the cavity perimeter, and (2) the negligible viscous pressure gradient outside the interface does not influence particles there, which helps us focus on the capillary compaction phenomenon only. For all simulations conducted here, we ensure that viscous

pressure drops are always smaller than 1% of capillary pressure drops, guaranteeing the dominance of capillary force in all fluid-fluid displacement processes.

In the two-way hydromechanical coupling, one needs to consider the disparity between the characteristic time steps of the fluid and granular mechanics algorithms. In particular, the characteristic pore volume for the granular pack, $V_{\text{pore}} \sim \frac{\pi d^2 h}{4} = 1.29 \times 10^{-11}$ m^3, at $\text{Ca}^* = 0.5$ results in the characteristic timescale for filling a single pore of 0.3 s. However, the characteristic timescale to capture the granular mechanics is $\Delta t_{\text{m}} \sim \sqrt{\frac{m}{K}} \sim 10^{-6}$ s. Matching granular mechanics and fluid time steps is computationally challenging since $\Delta t_{\text{fluid}} \sim 10^7 \times \Delta t_{\text{m}}$. Particles relax much faster than the characteristic time to invade a pore, so in our two-way coupling scheme we set $\frac{\Delta t_{\text{fluid}}}{\Delta t_{\text{m}}} \approx 2000$. This ratio is large enough to maintain computational efficiency, and small enough to ensure that particles have enough time to relax under calculated pressure forces between consecutive fluid time steps.

2.3 Model set-up

We simulate immiscible fluid-fluid displacement through a granular pack confined in a circular flow cell, by setting a constant injection rate at the center, and constant pressure at the perimeter. The invading and defending fluid viscosities are set to $\eta_{\text{inv}} = 8.9 \times 10^{-4}$ Pa$\cdot$s for water, and $\eta_{\text{def}} = 0.34$ Pa $\cdot$ s for oil, respectively, and the interfacial tension is set to $\gamma = 13 \times 10^{-3}$ N/m. These parameters are chosen to mimic the experiments of Zhao et al. [43]. The granular pack has an outer and inner radius of $R_{\text{out}} = 13.25$ mm, $R_{\text{in}} = 0.5$ mm, and a height $h = 330$ μm. We adopt a simplified Hertz–Mindlin contact model [51] for particles in the granular pack, with the following properties: shear modulus $G = 50$ MPa, Poisson ratio $\nu = 0.5$ (quasi-incompressible, as in [57]), coefficient of friction $\mu = 0.3$ [24], density $\rho = 1040$ kg/m^3, and mean diameter $d = 300$ μm with 10% standard deviation (the same polydispersity as in [57]). We choose an injection rate $Q_{\text{inj}} = 4.3 \times 10^{-11}$ m^3/s, corresponding to a modified capillary number $\text{Ca}^* = \eta_{\text{def}} Q_{\text{inj}} R_{\text{out}} / (\gamma h d^2) = 0.5$ [24], for which viscous pressure gradients have time to relax between front movements, and capillary effects govern the displacement [56]. We conduct simulations in which we fix these parameters, and we vary the contact angle θ from 140° (drainage) to 46° (imbibition), and the initial packing density ϕ_0 from 0.68 (loose pack) to 0.84 (dense pack).

2.4 Sample preparation

In this section, we describe the protocol for preparation of the granular pack in our simulations, and demonstrate that the proposed jamming phase diagram (FIG.4-3 in Chapter 4) is robust with respect to randomization of the initial packing. To generate an initial granular pack at a specific packing density ϕ_0, PFC2D [51] distributes particles with overlaps inside the outer boundary wall—the size of which we set to follow a Gaussian distribution with mean diameter $d = 300$ μm and 10% standard deviation. The particles are distributed evenly (uniform spatial distribution) throughout the model domain. This process ceases when the target packing fraction ϕ_0 (disregarding any overlap) is achieved. Then, we simulate cycles of mechanical interaction, during which period particles with prescribed properties (G, μ) rearrange themselves under contact forces, until equilibrium is reached. By changing the seed number for the the random-number generator, we obtain different initial packings at the same ϕ_0.

In Figure 2-2 we illustrate the robustness of the jamming analysis with respect to different realizations of the initial packing. We generate 5 different initial packings using different seeds for random number generation, for fixed $\phi_0 = 0.77$ and $\theta = 140^\circ$. While the precise patterns are of course different, they all exhibit the same morphological signature before and after jamming [Fig. 2-2(a)–(e)]. We confirm this lack of sensitivity of the jamming transition to the initial packing quantitatively. The evolution of the injection pressure P_{inj} is different for each simulation [Fig. 2-2(f)], but when we plot the mean particle stress P as a function of the packing fraction ϕ, the evolutions for all 5 realizations collapse on a single curve [Fig. 2-2(g)], leading to a critical packing density ϕ_c within the narrow range $[0.858, 0.865]$ and corresponding P^*_{inj} in the range of $[147.7, 179.2]$ Pa. Therefore, the trajectory on (P^*_{inj},$1/\phi$)-space (FIG.4-3 in Chapter 4) is virtually insensitive to the random generation of the initial granular packing.

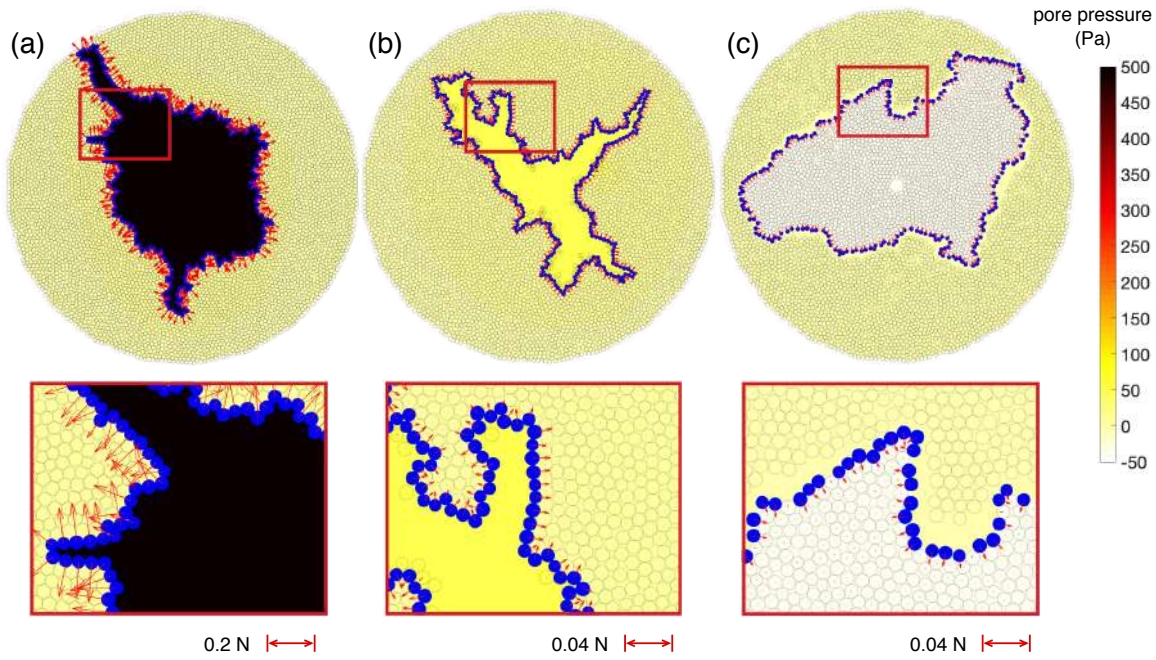

Figure 2-1: Interface morphology and pore pressure field at breakthrough for initial packing fraction $\phi_0 = 0.77$ and different wetting conditions: (a) $\theta = 140°$, (b) $\theta = 65°$, (c) $\theta = 46°$. Bottom: zoomed-in view of the particles near the interface, where red arrows indicate the resultant of pore pressure forces acting on each particle. Adapted from Meng et al. [2].

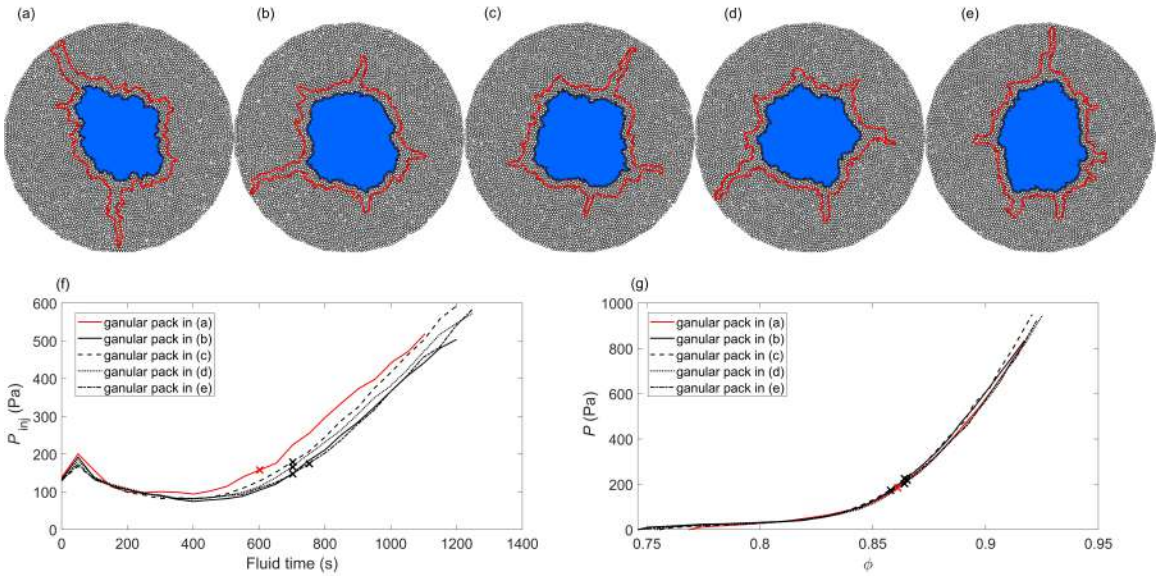

Figure 2-2: Jamming transition analysis for $\phi_0 = 0.77$, $\theta = 140°$. (a)-(e): Interface morphology at the jamming transition (black line) compared with that at breakthrough (red line) for five initial granular packs generated with different seed numbers; (f) Time evolution of injection pressure P_{inj}; and (g) Mean particle stress P as a function of packing density ϕ in the compacting granular layer for all five granular packs. Adapted from Meng et al. [2].

Chapter 3

Pattern formation and invasion dynamics

3.1 Evolution of interface morphology during fluid invasion

In Fig. 3-1, we show the fluid invasion morphologies that result from injection in the form of a visual phase diagram for different values of θ and ϕ_0. The collection of patterns at breakthrough—when the invading fluid first reaches the outer boundary—exhibits four different regimes: (I) cavity expansion and fracturing, (II) frictional fingers, (III) capillary invasion, and (IV) capillary compaction. In this section, we show and describe in detail the time evolution of the interface morphology and injection pressure for representative cases of each regime (Fig. 3-2; see also supplemental videos).

1. *Regime I: Cavity expansion and fracturing.* When the injection pressure from fluid injection is sufficient to push particles outwards, the cavity keeps expanding until the energy input becomes insufficient to compact the granular pack further; the point at which fractures emerge [Fig. 3-2(a)]. The displacement field is characterized by a petal-like structure, similar to what is observed in fluid-driven deformation processes in frictionless [57] or frictional [23, 24, 21] granular systems. The capillary pressure distribution demonstrates that the injected fluid always penetrates the widest throat with smallest associated capillary entry pressure (P_{cap}), and generally P_{cap} increases as the granular pack is being compacted. The wide range in P_{cap} at breakthrough ($t_d \to 1$) confirms the vulnerability of fracture tips ($P_{\text{cap}} \sim 450$ Pa) compared with

other throats along the cavity perimeter ($P_{\text{cap}} \sim 900$ Pa).

2. *Regime II: Frictional fingers.* At only weakly-wetting conditions, the injection pressure is positive but smaller than in drainage, and the energy input is insufficient to push particles in all directions and form a circular cavity. In this case, the injected fluid pushes away particles in certain directions, preferably those with loosely packed particles, and develops frictional fingers [Fig. 3-2(b)]. Such fingers develop also when injecting air into a mixture of grains and viscous fluid at low granular filling fraction, the characteristic width of which depends on the interplay between capillary and frictional forces [19, 23].

3. *Regime III: Capillary invasion.* When particles have been densely packed initially, a small injection pressure (either positive or negative) is insufficient to overcome the established chains of contact forces, and thus particles do not move. In this case, we observe patterns of capillary fluid invasion in rigid media [Fig. 3-2(c)], which are different under different wettabilities [37, 38, 41, 42, 43, 45, 46]. The crossover from capillary invasion to capillary fracturing depends on the competition between hydrodynamic driving forces and mechanical resisting forces. Such transition can be triggered by reducing the confining weight, and hence frictional resistance [24], or, as we demonstrate here, by increasing θ to increase capillary forces.

4. *Regime IV: Capillary compaction.* In strong imbibition the injection pressure is negative, and for sufficiently loose granular packs, particles are dragged into the invading fluid under the out-of-plane curvature effect, leading to capillary compaction [Fig. 3-2(d)]. Given the relatively small magnitude of the dragging suction pressure (~ -30 Pa), the compacted packing density inside the fluid-fluid interface remains nearly the same for granular packs with different ϕ_0.

3.2 Particle displacement field at breakthrough

The total particle displacement field presented in Figure 3-3 shows that the granular pack is compacted to a denser state as θ increases, since the higher injection pressure provides the energy needed to mobilize and rearrange particles in a larger region. For the cases where $\theta \geq 65^\circ$, fracture tips always locate in low packing density (η) regions with lower

$P_{capEntry}$ compared with other interface particles. The magnitude of total displacement demonstrates a decreasing trend from the cavity to the rigid boundary, with a pedal-like mesoscale structure. Similar pedal-like structures have been observed in other systems, where the fluid is injected into initially dry packing of frictional particles [**?**], or saturated packing of soft, slippery particles [57].

3.3 Invasion events analysis

Previous study on invasion events happened in fluid-fluid displacement process shows that in drainage condition ($\theta = 160°$), "burst" event dominates, and in imbibition ($\theta = 46° \sim 60°$), "touch" and "overlap" events take over [45]. Here, by studying the movable granular pack, it is found that particle movement under different wetting conditions influences the signature of invasion events significantly (Fig. 3-4). Initially, particles are pushed outwards and the interface is stretched, the tendency to incorporate nearby particles to fill gaps along the interface dictates the dominance of "touch" event. With more particles incorporated into the interface, interface particles are squeezed and in good contact with neighbors, leading to a transition from "touch" to "burst" event (Fig. 3-4(b)(c)). When θ decreases from $120° \sim 65°$, there is an overall transition from "burst" to cooperative filling events ("touch", "overlap"), which is in line with Primkulov et al. [45] results. The position of an invasion event is analyzed by calculating the angle (θ) formed by the interface particle where the event takes place and its neighbors, and thus events happen at fracture tips have $\theta \leq 60°$, at concave regions along fracture sides have $\theta \geq 180°$. Figure 3-4 shows that fracture tip advances through "burst" event at $\theta = 120°$, "burst" and "touch" events at $\theta = 75°$, and mostly "touch" event at $\theta = 65°$. "Overlap" event only happens at concave regions along fracture sides ($\theta \sim 300°$), which is also confirmed by looking at positions of the trapped particles inside the cavity. Lastly, in drainage condition fewer invasion events take place, because most of the injecting fluid is consumed by filling the cavity created by particle movements, instead of filling pores and triggering invasion events.

3.4 Signals of injection pressure and packing density

The temporal signal of the injection pressure encodes information needed to understand the interplay between particle movement and fluid-fluid displacement. Since we restrict

our study to the case when capillary forces dominate and viscous dissipation is negligible, the injection pressure signal is determined by the capillary entry pressure P_{cap}, which is a sum of in-plane and out-of-plane components. As a result, the injection pressure shows fluctuations in a stick-slip manner for all θ and ϕ_0, as has been documented in slow drainage experiments [58, 56, 59] and simulations [46]. As θ decreases, indicating that the substrate becomes more wetting to the invading fluid, the fluid-fluid displacement is controlled by cooperative pore-filling events (touch and overlap) with smaller P_{cap} compared with burst events [37, 38, 45, 46]. This explains the general decreasing trend of injection pressure as θ decreases [Fig. 3-5(a)].

In a drainage displacement, instead of fluctuating around a mean value [46], the injection pressure exhibits a surprising convex shape as a function of time, first decreasing and then increasing with time. This is a signature of the fluid-solid coupling: the particles around the cavity are separated (opening up the throats and decreasing P_{cap}) during the initial stages of expansion, and then brought closer together (narrowing the throats and increasing P_{cap}), as the granular pack is being compacted during the late stages [Fig. 3-5(a)].

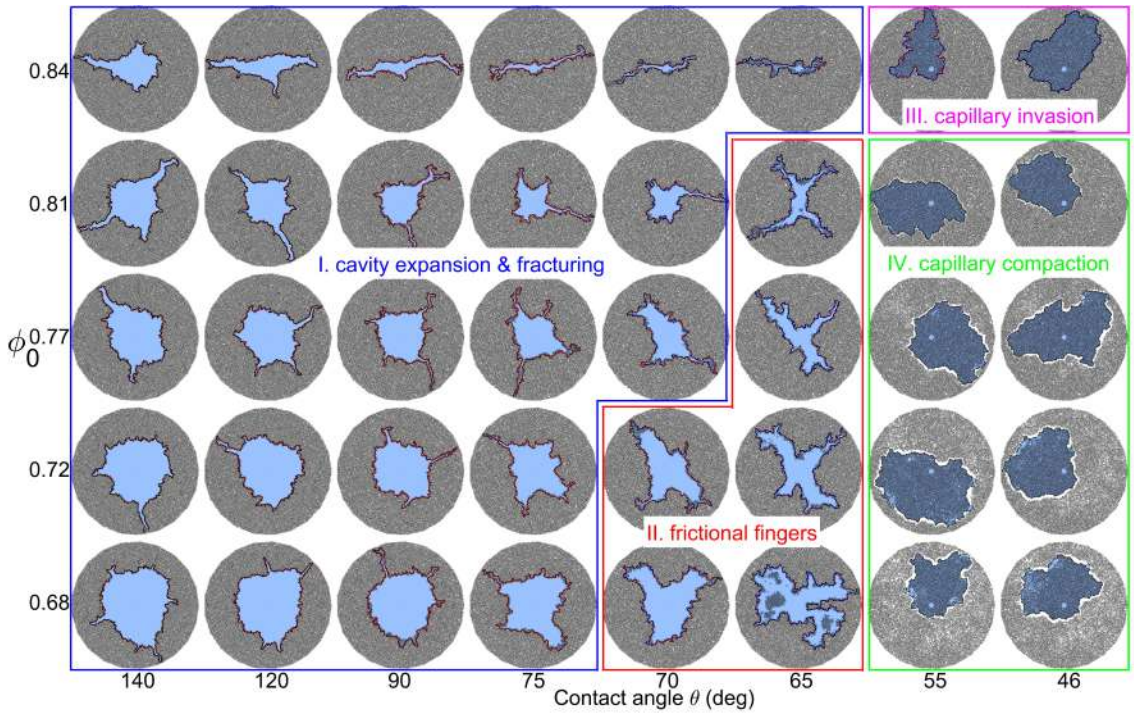

Figure 3-1: Visual phase diagram of the invading fluid morphology at breakthrough corresponding to different substrate wettabilities (contact angle θ) and initial packing densities ϕ_0. We identify four distinct morphological regimes: (I) cavity expansion and fracturing, (II) frictional fingers, (III) capillary invasion, and (IV) capillary compaction. Adapted from Meng et al. [2].

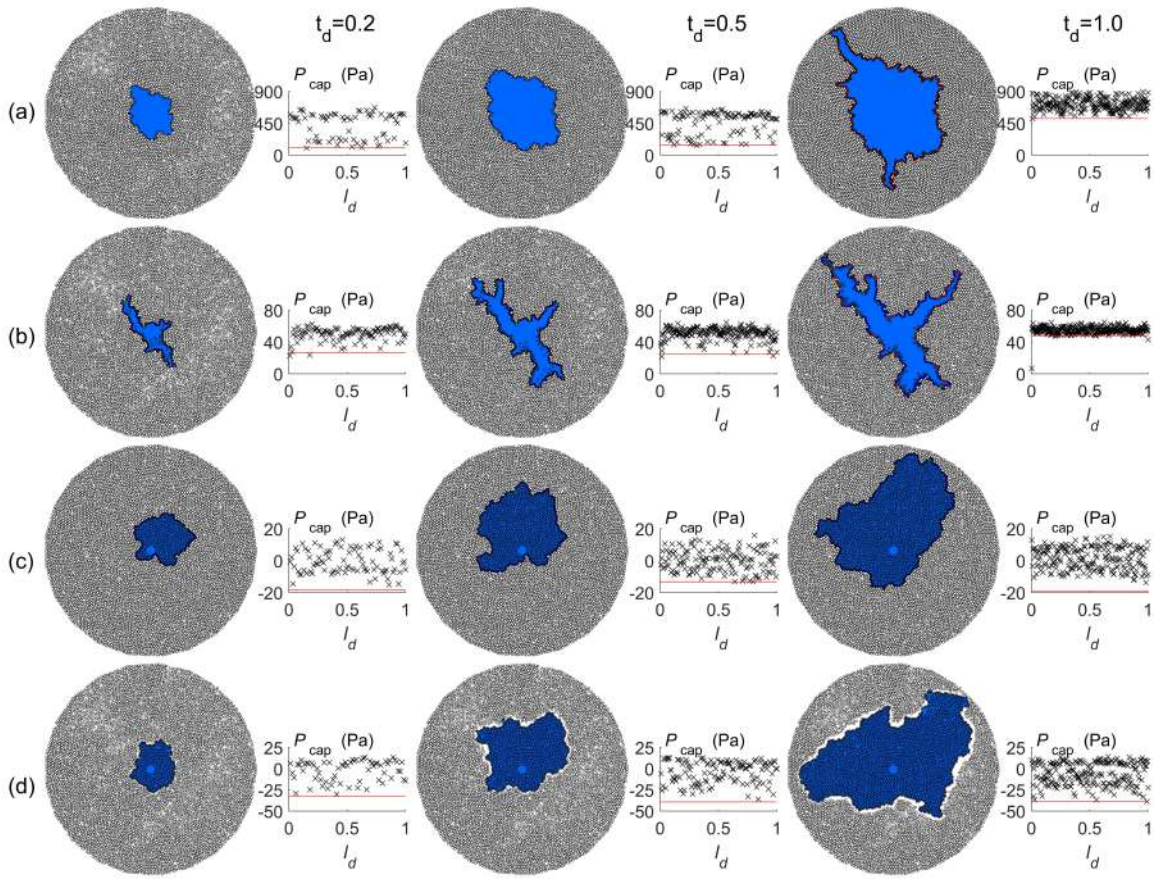

Figure 3-2: Evolution of interface morphology at $t_d(= t/t_{\text{breakthrough}}) = 0.2, 0.5, 1.0$. The insets show the capillary entry pressure (P_{cap}) for every throat at the fluid-fluid interface (black crosses) and the injection pressure at that moment (red line). (a) Cavity expansion and fracturing (regime I), $\phi_0 = 0.77, \theta = 140°$. (b) Frictional fingers (regime II), $\phi_0 = 0.77, \theta = 65°$. (c) Capillary invasion (regime III), $\phi_0 = 0.84, \theta = 46°$. (d) Capillary compaction (regime IV), $\phi_0 = 0.77, \theta = 46°$. Adapted from Meng et al. [2].

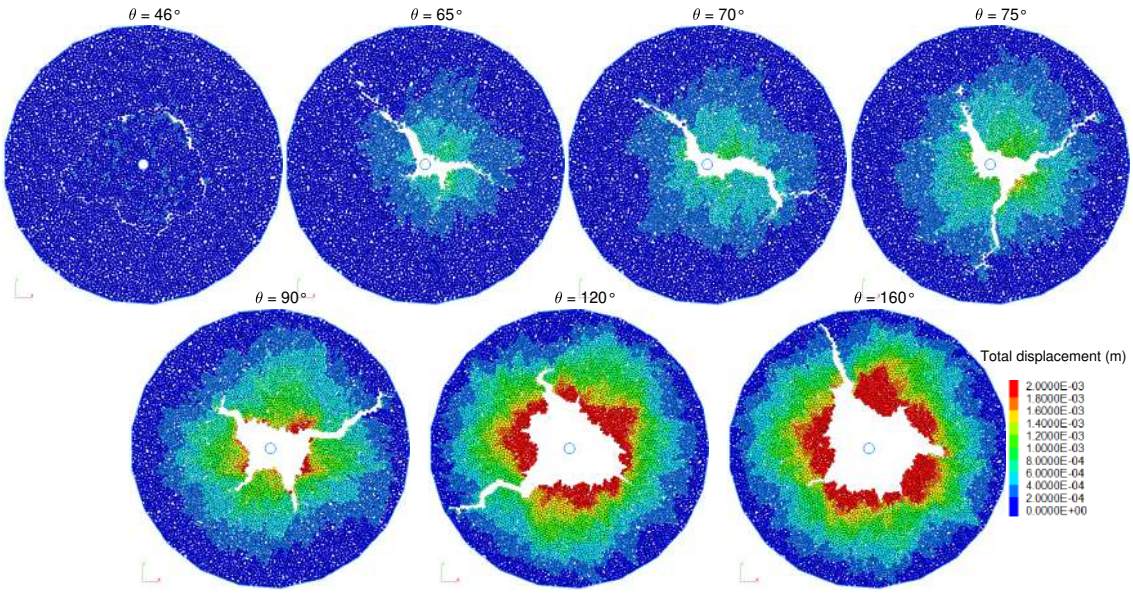

Figure 3-3: Comparison of total particle displacement fields that develop under different wettability conditions.

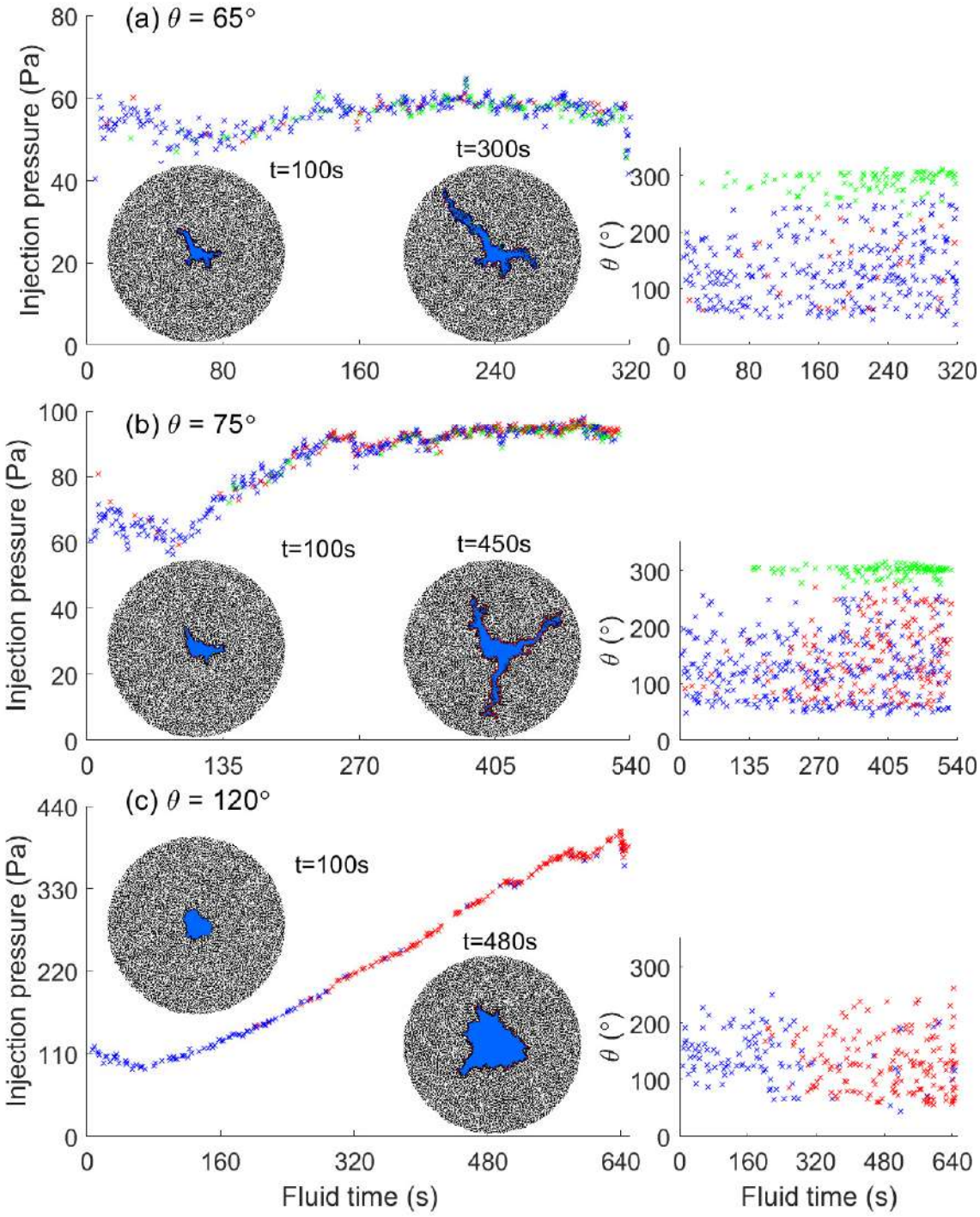

Figure 3-4: Temporal profiles of invasion events happened throughout the process (red, blue, green cross represents burst, touch, overlap event separately). The vertical axis for the left, and right profile shows the injection pressure when an event happens, and the angle (θ) formed by the particle where the event happens and its two neighboring particles. The profiles for three contact angles are shown here: $(a)\theta = 65°.(b)\theta = 75°.(c)\theta = 120°$.

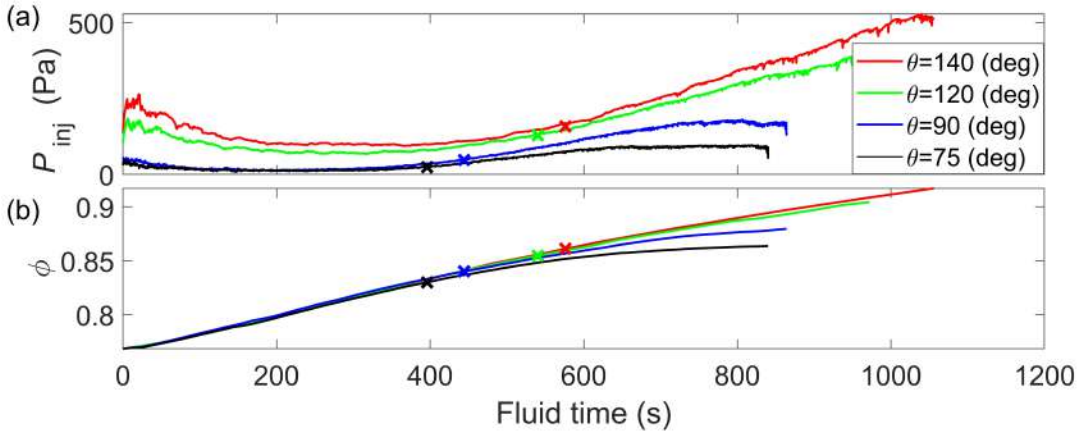

Figure 3-5: Time evolution of (a) injection pressure P_{inj}, and (b) packing density ϕ, for simulations with initial packing density $\phi_0 = 0.77$, and $\theta = 75°, 90°, 120°, 140°$. The crosses denote the jamming transition for each case. Adapted from Meng et al. [2].

THIS PAGE INTENTIONALLY LEFT BLANK

Chapter 4

Mechanism behind emergence of fracturing: jamming transition

Figure 3-1 exhibits a surprising and heretofore unrecognized behavior of fluid injection into a granular pack: a decrease in θ—that is, transitioning from drainage to weak imbibition—leads to earlier onset of fracturing, as evidenced by the smaller size of the fluid cavity at fluid breakthrough. This behavior cannot be explained by the evolving injection pressure level, or the evolving packing fraction outside the cavity, or the volume of fluid injected alone. Indeed, the transition to fracturing for different wetting conditions occurs at different injection pressures [Fig. 3-5(a)], different packing fractions [Fig. 3-5(b)], and different times [Fig. 3-5(a),(b)].

This raises the question of how wettability impacts the onset of fracturing, and whether such dependence is amenable to prediction. To answer this question, we hypothesize that the emergence of fracturing is akin to a phase transition from liquid-like to solid-like behavior, and that, therefore, it can be understood as a *jamming transition*. Indeed, the jamming transition has proved instrumental in understanding mechanical integrity in a remarkably diverse range of systems [60]. Examples include colloidal suspensions [61], athermal systems such as foam and emulsions [62], and the glass transition in supercooled liquids [63, 64]. The jamming transition also occurs in (dry) granular systems at a well-defined packing density ϕ_c when the conditions of mechanical stability are satisfied [65, 66, 67, 68, 69, 68]. Here we explore whether the concept of jamming can be used to quantitatively explain the emergence of fractures in *wet* granular systems and, specifically, whether the onset of fracturing in our

system arises from a jamming transition.

4.1 Jamming transition analysis from classic metrics

The jamming transition in a dry granular system occurs at a threshold packing fraction, ϕ_c, when mechanical stability is achieved. For $\phi < \phi_c$, the network of contact forces is constantly evolving and changing topology through particle rearrangement. For $\phi > \phi_c$, in contrast, the force network locks in and its strength is enhanced through particle deformation [68, 65]. Classic metrics that characterize the transition in frictionless systems are a discontinuous increase in the mean contact number Z, a rise in the mean isotropic stress P of the granular pack above its background value [65], or the emergence of a nonzero shear modulus [67].

We confirm that the behavior of our system responds in a manner consistent with a jamming transition. In particular, we compute at each stage of the granular pack deformation the Cauchy stress tensor for each particle in the system, $\sigma_{ij} = \frac{1}{V}\sum_{n_c}(x_i^c - x_i)F_j^c$, where n_c is the number of contacts for the particle. From the stress tensor we extract its isotropic component $P = \mathrm{tr}(\sigma_{ij})$ and a measure of the shear stress, $\tau_{\max} = (\sigma_{\max} - \sigma_{\min})/2$, where $\sigma_{\max}$ and $\sigma_{\min}$ are the largest and smallest eigenvalues of σ_{ij}, respectively. We observe that both quantities rise above a near-zero background as a function of the evolving mean packing fraction ϕ outside the central cavity [Fig. 4-1(a)].

We determine the jamming transition ϕ_c from the $\tau_{\max}$ profile as the intersection of two straight lines: one fitting the response of the background state, and one fitting a straight line to the asymptotic behavior in the highly compacted state [65, 67] [Fig. 4-1(a), top inset]. For simulations with initial packing density $\phi_0 = 0.77$, the jamming transition occurs at a critical packing density ϕ_c that takes increasing values (between 0.83 and 0.86) for increasing values of the contact angle (between $\theta = 75^\circ$ and 140°) [Fig. 4-1(a)]. This result is consistent with our hypothesis of the emergence of fracturing being controlled by a jamming transition, in which the transition occurs earlier (at a smaller ϕ_c) in imbibition than in drainage. Previous studies of jamming transition in both frictionless [70, 71, 68] and frictional [65] systems show a power-law increase of the mean stress with packing fraction above jamming, $P - P_c \sim (\phi - \phi_c)^\psi$, with an exponent slightly larger than 1, $\psi \approx 1.1$. Our simulations for wet granular system also show a power-law increase, with the exponent ψ in the range 1.06–1.39, larger values corresponding to drainage displacements and loose granular packs, and

smaller values corresponding to imbibition displacements and dense granular packs [Fig. 4-1(b), middle inset]. For our granular packings of finite $\mu = 0.3$, Z_c is expected to vary smoothly between $Z_c(\mu = 0) = 4$ and $Z_c(\mu \to \infty) \to 3$ [72, 71]. Indeed, we find that Z_c lies in the range of $3.49 \sim 3.96$, and exhibits a power-law dependence with packing fraction above jamming, $Z - Z_c \sim (\phi - \phi_c)^\beta$, $\beta \sim 0.87$ [Fig. 3(c), bottom inset]. Previous research determines exponents in jamming at the vicinity of the jamming packing fraction and shows that $\beta \sim 0.5$ [71, 65, 73, 68, 74]. Here we also study behaviors of the granular packs after the jamming transition, and thus a correction-to-scaling analysis is conducted [75, 76]: $Z - Z_c = (\phi - \phi_c)^\beta(1 + a(\phi - \phi_c)^\omega + \dots)$, with the leading correction-to-scaling exponent $\omega = 0.3$ [75], and the prefactor $a = 8.94$ in the order of $O(1)$, which validates the β we obtained. The fact that fractures grow after the defined jamming transition ϕ_c (as evidenced by a visual comparison of the interface morphology at jamming and at breakthrough [Fig. 4-1(d)]) confirms our hypothesis that the onset of fractures emerges from a jamming transition.

4.2 Microscopic evidence for jamming transition: evolution of the contact force network

As stated in last section, the jamming transition occurs in granular systems at a well-defined packing density ϕ_c, when the particles form force chains along the compression direction [61], and the conditions of mechanical stability are satisfied [65, 66, 67, 68, 69]. Figure 4-2 demonstrates the evolution of the contact-force network for $\phi_0 = 0.77$, $\theta = 140°$. Before the jamming transition [Fig. 4-2(a),(b)], the granular pack behaves in a fluid-like manner, with particles being rearranged, and force chains being broken-up and rebuilt intermittently. The jamming transition ϕ_c has been determined from the $(\tau_{\max} - \phi)$ profile. At the jamming transition [Fig. 4-2(c)], force chains have been developed radially to resist the injection pressure, and the system reaches mechanical stability. After the jamming transition [Fig. 4-2(d),(e)], the granular pack behaves in a solid-like manner, with fractures growing, and the established force chains being reinforced in strength.

4.3 Phase diagram of jamming for wet granular media

A fundamental contribution to understanding jamming in (dry) granular systems was made in the form of a phase diagram that delineates the jammed state in the phase space of density, load and temperature [77]. It shows that jamming can occur only at sufficiently high density, and that an increase in either load or temperature can unjam a system. We extend this description to wet granular systems by identifying quantities that determine the phase transition between jammed and unjammed states. We identify the packing fraction ϕ as the "density", and we posit that injection pressure P_{inj} plays the role of the "load" during injection. Thus, we represent any generic evolution of our system as a *trajectory* in $(P^*_{\text{inj}}, 1/\phi)$-space (Fig. 4-3), where P_{inj} is nondimensionalized by the characteristic capillary entry pressure in the system, γ/d.

Trajectories for regime I start with the prescribed ϕ_0 and move upwards in phase space as the granular pack is being compacted by the injected fluid. The injection pressure shows an initially-decreasing and then-increasing trend, as explained in Fig. 3-5(a). The transition from cavity expansion to fracturing corresponds to a transition from the unjammed state to the jammed state. We collect transition points ϕ_c (shown as red markers in Fig. 4-3) for every simulation with a specific ϕ_0 and θ. These points collapse on a line in $(P^*_{\text{inj}}, 1/\phi)$-space, showing that under the same loading condition, the system jams at the same ϕ_c, independently of θ or ϕ_0. This transition line in the jamming phase diagram separates fundamentally different behaviors exhibited by our wet granular systems: fluid-like behavior (cavity expansion) in the unjammed state, and solid-like behavior (fracturing) in the jammed state (Fig. 4-3). This transition also helps explain the onset of fracturing: a larger energy input brought by the injection of a nonwetting fluid (larger value of the contact angle θ) compacts the system to a denser state before jamming occurs, which, in turn, delays the onset of fracturing.

We also show in Fig. 4-3 the trajectories for regimes II, III and IV. Frictional fingers (regime II) have positive injection pressure. The trajectories corresponding to this regime move upwards in ϕ as the system is being compacted, with stick-slip fluctuations in P_{inj}, but remain in the unjammed state for their entire evolution. Capillary invasion (regime III) occurs in an initially dense granular pack. The entire trajectory lies in the jammed state, with almost-constant ϕ and stick-slip fluctuations in P_{inj}. Capillary compaction (regime IV)

occurs when the out-of-plane capillary pressure dominates and the granular pack is relatively loose initially. We calculate ϕ for the region inside the fluid-fluid interface. Since the negative dragging pressure is comparable for all our simulations in this regime (-50 Pa to -10 Pa), the granular pack is compacted inwards up to approximately the same packing density ($\phi \approx 0.83$) above the jamming transition. At zero external load ($P_{\text{inj}} = 0$), our system jams at the random close packing fraction $\phi_c \approx \phi_{\text{rcp}} \approx 0.84$ [78, 79, 80].

4.4 Influence of grain properties on the jamming phase diagram

The jamming phase diagram delineated holds under different values of the system parameters. To illustrate this robustness, we have explored the influence of changing the value of the coefficient of friction μ and the shear modulus G (the aforementioned simulations correspond to $\mu = 0.3$ and $G = 50$ MPa). We find that the jamming transition shifts towards *higher* values of packing fraction ϕ_c as μ decreases [Fig. 4-4(a)] and also as G decreases [Fig. 4-4(b)]. These results confirm that when the particles of the granular pack are either less frictional or softer, the system jams at a denser state.

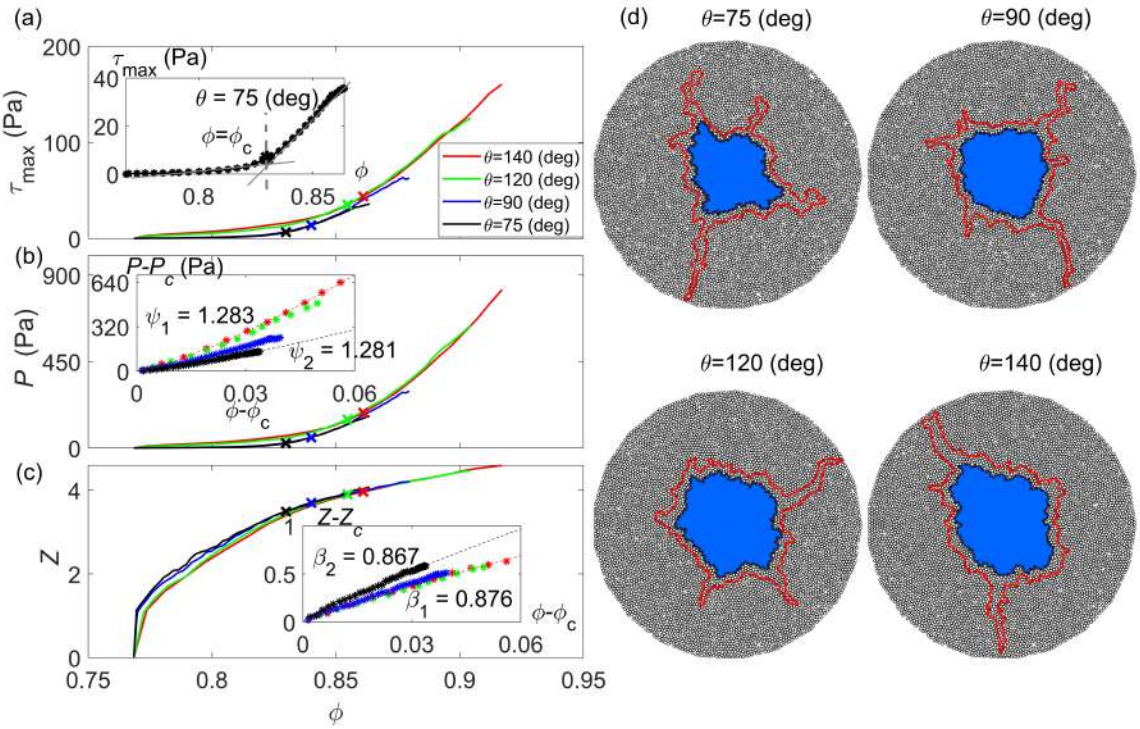

Figure 4-1: Jamming transition analysis for $\phi_0 = 0.77$, $\theta = 75°, 90°, 120°, 140°$. (a)-(c) Average maximum shear stress ($\tau_{\max}$), mean particle stress (P), and mean contact number (Z) as a function of packing density ϕ in the compacting granular layer. (a) inset: determination of the critical packing fraction at jamming. (b),(c) insets: $P - P_c$, $Z - Z_c$ as a function of $\phi - \phi_c$, exhibiting power-law trends; (d) Interface morphology at the jamming transition [identified from (a)] for $\theta = 75°, 90°, 120°, 140°$ (black line), compared with that at breakthrough (red line). The comparison confirms that the jamming transition determines the onset of fracturing. Adapted from Meng et al. [2].

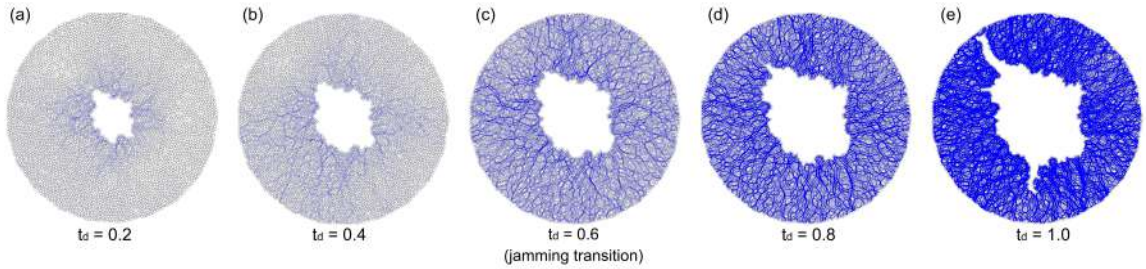

Figure 4-2: Evolution of the contact-force network for $\phi_0 = 0.77$, $\theta = 140°$, at (a) $t_d = 0.2$, (b) $t_d = 0.4$, (c) $t_d = 0.6$ (jamming transition), (d) $t_d = 0.8$, and (e) $t_d = 1.0$. The thickness of the blue line is proportional to the magnitude of the interparticle force. Adapted from Meng et al. [2].

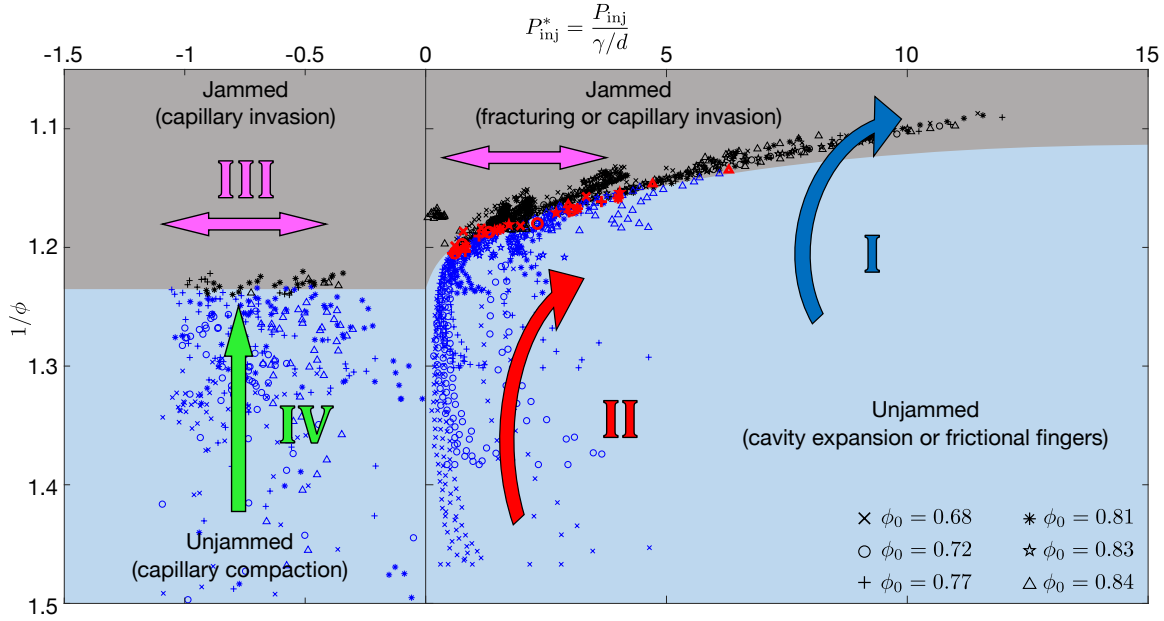

Figure 4-3: Phase diagram of jamming for wet granular media when capillary forces dominate. Shown are the trajectories of the system in $(P^*_{\mathrm{inj}}, 1/\phi)$-space for all the simulated cases of Fig. 3-1, ranging in contact angle θ from 140° (drainage) to 46° (imbibition), and ranging in initial packing density ϕ_0 from 0.68 (loose pack) to 0.84 (dense pack). Note the different scale of the horizontal axis for positive and negative injection pressures. For all four regimes of fluid invasion and grain deformation, the proposed diagram uniquely separates the system's unjammed state (blue) from its jammed state (gray), independently of θ and ϕ_0. In particular, this explains the onset of fracturing in capillary-dominated fluid-driven injection into granular packs (red symbols). Adapted from Meng et al. [2].

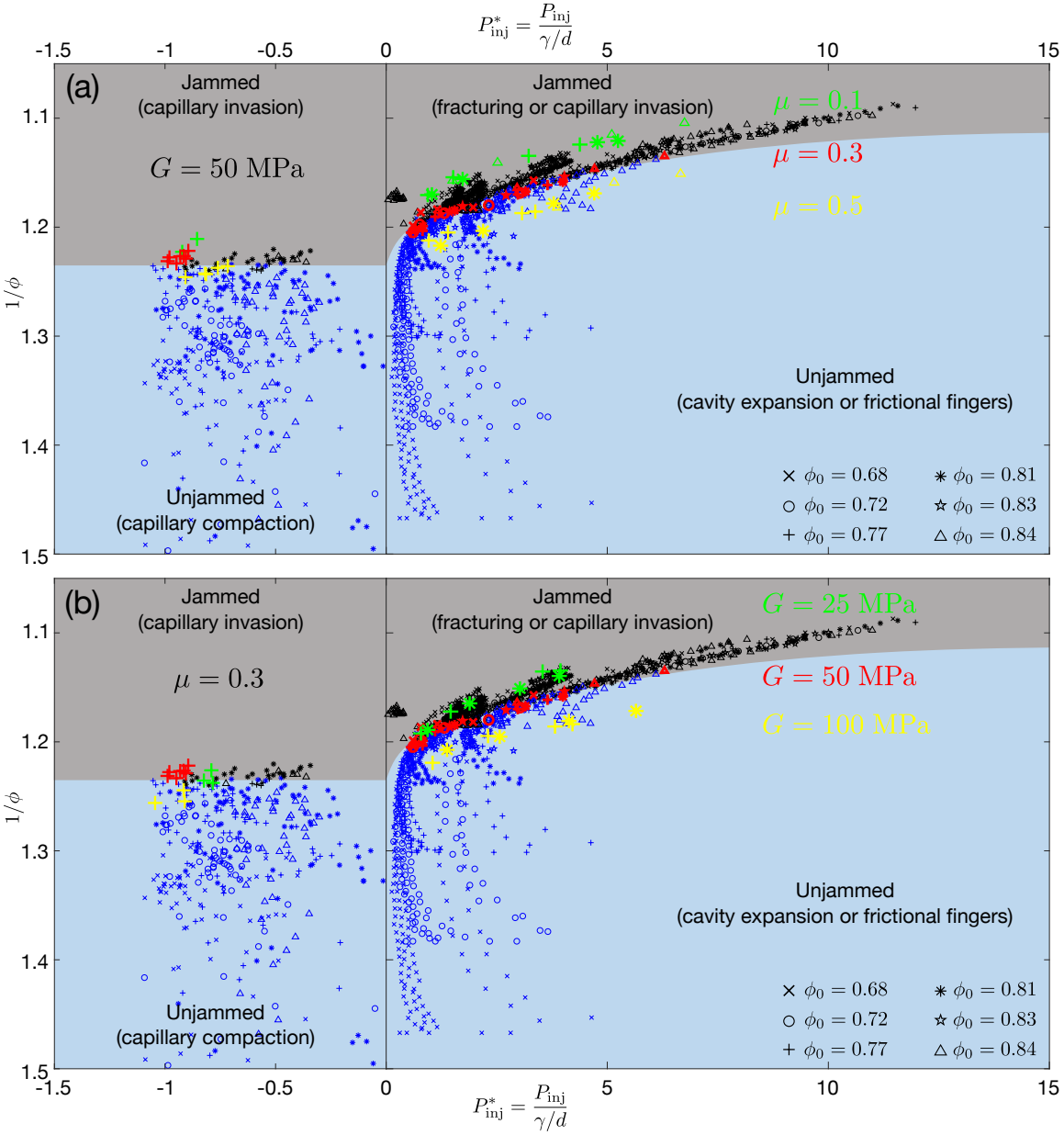

Figure 4-4: Influence of grain properties on the jamming phase diagram for wet granular media when capillary forces dominate. (a) Coefficient of friction taking values $\mu = 0.1$, 0.3 and 0.5, (b) Shear modulus taking values $G = 25$, 50 and 100 MPa. Adapted from Meng et al. [2].

Chapter 5

Conclusion

In summary, we have studied morphological transitions in granular packs as a result of capillary-dominated fluid-fluid displacement via a novel, fully-coupled model of two-phase flow and grain mechanics. Simulations of fluid injection into a granular pack with different initial packing densities and substrate wettabilities have led to uncovering four invasion regimes: cavity expansion and fracturing, frictional fingers, capillary invasion, and capillary compaction. In particular, we have identified the emergence of fracture, and its surprising and unexplored dependence on the system's wettability. We have shown that the onset of fracture can be explained as a jamming transition, as confirmed by the behavior of classic metrics of jamming such as the mean isotropic stress. We have synthesized the system's response in the form of a phase diagram of jamming for wet granular media, on which the jamming transition for all different trajectories collapse on a single line in $(P^*_{\text{inj}}, 1/\phi)$-space, independently of the initial packing density ϕ_0 and contact angle θ.

Our study paves the way for understanding the impact of other key variables of a wet granular system, such as properties of the solid particles (rigidity, friction coefficient, cementation) or the fluid (viscosity contrast, capillary number). By tailoring the range of values of these variables, our analysis may provide fundamental insight on specific applications, from nanotechnology [81] to energy recovery [82], natural gas seeps [83, 84] and geohazards [85, 86].

THIS PAGE INTENTIONALLY LEFT BLANK

Bibliography

[1] M. Trojer, P. de Anna, and R. Juanes. Impact of wetting on fracturing of granular media. *Submitted for publication.*

[2] Yue Meng, Bauyrzhan K Primkulov, Zhibing Yang, Chung Yee Kwok, and Ruben Juanes. Jamming transition and emergence of fracturing in wet granular media. *Physical Review Research*, 2(2):022012, 2020.

[3] Luis Cueto-Felgueroso and Ruben Juanes. Nonlocal interface dynamics and pattern formation in gravity-driven unsaturated flow through porous media. *Physical Review Letters*, 101(24):244504, 2008.

[4] Michael L Szulczewski, Christopher W MacMinn, Howard J Herzog, and Ruben Juanes. Lifetime of carbon capture and storage as a climate-change mitigation technology. *Proceedings of the National Academy of Sciences*, 109(14):5185–5189, 2012.

[5] James W Mercer and Robert M Cohen. A review of immiscible fluids in the subsurface: properties, models, characterization and remediation. *Journal of Contaminant Hydrology*, 6(2):107–163, 1990.

[6] F M Orr and JJ Taber. Use of carbon dioxide in enhanced oil recovery. *Science*, 224 (4649):563–569, 1984.

[7] Rémi Dangla, Sungyon Lee, and Charles N Baroud. Trapping microfluidic drops in wells of surface energy. *Physical Review Letters*, 107(12):124501, 2011.

[8] Eric Brown and Heinrich M Jaeger. Shear thickening in concentrated suspensions: phenomenology, mechanisms and relations to jamming. *Reports on Progress in Physics*, 77(4):046602, 2014.

[9] Rausan Jewel, Andreea Panaitescu, and Arshad Kudrolli. Micromechanics of intruder motion in wet granular medium. *Physical Review Fluids*, 3(8):084303, 2018.

[10] Eric R Dufresne, Eric I Corwin, NA Greenblatt, Jacqueline Ashmore, DY Wang, Anthony D Dinsmore, JX Cheng, XS Xie, John W Hutchinson, and David A Weitz. Flow and fracture in drying nanoparticle suspensions. *Physical Review Letters*, 91(22):224501, 2003.

[11] Dominic Vella, Pascale Aussillous, and L Mahadevan. Elasticity of an interfacial particle raft. *EPL (Europhysics Letters)*, 68(2):212, 2004.

[12] AK Jain and R Juanes. Preferential mode of gas invasion in sediments: Grain-scale mechanistic model of coupled multiphase fluid flow and sediment mechanics. *Journal of Geophysical Research: Solid Earth*, 114:B08101, 2009.

[13] Hosung Shin and J Carlos Santamarina. Fluid-driven fractures in uncemented sediments: Underlying particle-level processes. *Earth and Planetary Science Letters*, 299 (1-2):180–189, 2010.

[14] Lucas Goehring, William J Clegg, and Alexander F Routh. Plasticity and fracture in drying colloidal films. *Physical Review Letters*, 110(2):024301, 2013.

[15] Christian Peco, Wei Chen, Yingjie Liu, MM Bandi, John E Dolbow, and Eliot Fried. Influence of surface tension in the surfactant-driven fracture of closely-packed particulate monolayers. *Soft Matter*, 13(35):5832–5841, 2017.

[16] Zhonghao Sun and J Carlos Santamarina. Grain-displacive gas migration in fine-grained sediments. *Journal of Geophysical Research: Solid Earth*, 124(3):2274–2285, 2019.

[17] A. Groisman and E. Kaplan. An experimental study of cracking induced by desiccation. *Europhysics Letters*, 25(6):415–420, 1994.

[18] H. Shin and J. C. Santamarina. Desiccation cracks in saturated fine-grained soils: particle-level phenomena and effective-stress analysis. *Geotechnique*, 61(11):961–972, 2011.

[19] Bjornar Sandnes, HA Knudsen, KJ Måløy, and EG Flekkøy. Labyrinth patterns in confined granular-fluid systems. *Physical Review Letters*, 99(3):038001, 2007.

[20] Xiang Cheng, Lei Xu, Aaron Patterson, Heinrich M Jaeger, and Sidney R Nagel. Towards the zero-surface-tension limit in granular fingering instability. *Nature Physics*, 4 (3):234, 2008.

[21] Haiying Huang, Fengshou Zhang, Patrick Callahan, and Joseph Ayoub. Granular fingering in fluid injection into dense granular media in a hele-shaw cell. *Physical Review Letters*, 108(25):258001, 2012.

[22] Fengshou Zhang, Branko Damjanac, and Haiying Huang. Coupled discrete element modeling of fluid injection into dense granular media. *Journal of Geophysical Research: Solid Earth*, 118(6):2703–2722, 2013.

[23] Bjornar Sandnes, EG Flekkøy, HA Knudsen, KJ Måløy, and H See. Patterns and flow in frictional fluid dynamics. *Nature Communications*, 2:288, 2011.

[24] Ran Holtzman, Michael L Szulczewski, and Ruben Juanes. Capillary fracturing in granular media. *Physical Review Letters*, 108(26):264504, 2012.

[25] Fredrik K Eriksen, Renaud Toussaint, Knut J Måløy, and Eirik G Flekkøy. Invasion patterns during two-phase flow in deformable porous media. *Frontiers in Physics*, 3:81, 2015.

[26] Ran Holtzman and Ruben Juanes. Crossover from fingering to fracturing in deformable disordered media. *Physical Review E*, 82(4):046305, 2010.

[27] Germán Varas, Valérie Vidal, and Jean-Christophe Géminard. Venting dynamics of an immersed granular layer. *Physical Review E*, 83(1):011302, 2011.

[28] Germán Varas, Valérie Vidal, and Jean-Christophe Géminard. Morphology of air invasion in an immersed granular layer. *Physical Review E*, 83(6):061302, 2011.

[29] Sungyon Lee, Jeremy Lee, Robin Le Mestre, Feng Xu, and Christopher W MacMinn. Capturing gas in a soft granular material. *arXiv preprint arXiv:1808.02921*, 2018.

[30] Bernard P Boudreau, Chris Algar, Bruce D Johnson, Ian Croudace, Allen Reed, Yoko Furukawa, Kelley M Dorgan, Peter A Jumars, Abraham S Grader, and Bruce S Gardiner. Bubble growth and rise in soft sediments. *Geology*, 33(6):517–520, 2005.

[31] Benjamin P Scandella, Liam Pillsbury, Thomas Weber, Carolyn Ruppel, Harold F Hemond, and Ruben Juanes. Ephemerality of discrete methane vents in lake sediments. *Geophysical Research Letters*, 43(9):4374–4381, 2016.

[32] Benjamin P Scandella, Charuleka Varadharajan, Harold F Hemond, Carolyn Ruppel, and Ruben Juanes. A conduit dilation model of methane venting from lake sediments. *Geophysical Research Letters*, 38(6):L06408, 2011.

[33] Benjamin P Scandella, Kyle Delwiche, Harold F Hemond, and Ruben Juanes. Persistence of bubble outlets in soft, methane-generating sediments. *Journal of Geophysical Research: Biogeosciences*, 122(6):1298–1320, 2017.

[34] James C Melrose et al. Wettability as related to capillary action in porous media. *Society of Petroleum Engineers Journal*, 5(03):259–271, 1965.

[35] Irving Fatt, Waldemar A Klikoff Jr, et al. Effect of fractional wettability on multiphase flow through porous media. *Journal of Petroleum Technology*, 11(10):71–76, 1959.

[36] Martin J Blunt and Harvey Scher. Pore-level modeling of wetting. *Physical Review E*, 52(6):6387, 1995.

[37] Marek Cieplak and Mark O Robbins. Dynamical transition in quasistatic fluid invasion in porous media. *Physical Review Letters*, 60(20):2042, 1988.

[38] Marek Cieplak and Mark O Robbins. Influence of contact angle on quasistatic fluid invasion of porous media. *Physical Review B*, 41(16):11508, 1990.

[39] Martin J Blunt. Flow in porous media—pore-network models and multiphase flow. *Current Opinion in Colloid and Interface Science*, 6(3):197–207, 2001.

[40] P. H. Valvatne and M. J. Blunt. Predictive pore-scale modeling of two-phase flow in mixed wet media. *Water Resources Research*, 40:W07406, 2004.

[41] Mathias Trojer, Michael L Szulczewski, and Ruben Juanes. Stabilizing fluid-fluid displacements in porous media through wettability alteration. *Physical Review Applied*, 3 (5):054008, 2015.

[42] Ran Holtzman and Enrico Segre. Wettability stabilizes fluid invasion into porous media via nonlocal, cooperative pore filling. *Physical Review Letters*, 115(16):164501, 2015.

[43] Benzhong Zhao, Christopher W MacMinn, and Ruben Juanes. Wettability control on multiphase flow in patterned microfluidics. *Proceedings of the National Academy of Sciences*, 113(37):10251–10256, 2016.

[44] Michael Jung, Martin Brinkmann, Ralf Seemann, Thomas Hiller, Marta Sanchez de La Lama, and Stephan Herminghaus. Wettability controls slow immiscible displacement through local interfacial instabilities. *Physical Review Fluids*, 1(7):074202, 2016.

[45] Bauyrzhan K Primkulov, Stephen Talman, Keivan Khaleghi, Alireza Rangriz Shokri, Rick Chalaturnyk, Benzhong Zhao, Christopher W MacMinn, and Ruben Juanes. Quasistatic fluid-fluid displacement in porous media: Invasion-percolation through a wetting transition. *Physical Review Fluids*, 3(10):104001, 2018.

[46] Bauyrzhan K Primkulov, Amir A Pahlavan, Xiaojing Fu, Benzhong Zhao, Christopher W MacMinn, and Ruben Juanes. Signatures of fluid-fluid displacement in porous media: wettability, patterns, and pressures. *Journal of Fluid Mechanics*, 875:R4, 2019.

[47] Ahmed AlRatrout, Martin J Blunt, and Branko Bijeljic. Wettability in complex porous materials, the mixed-wet state, and its relationship to surface roughness. *Proceedings of the National Academy of Sciences*, 115(36):8901–8906, 2018.

[48] M Rücker, W-B Bartels, Kamaljit Singh, N Brussee, A Coorn, HA van der Linde, A Bonnin, H Ott, SM Hassanizadeh, MJ Blunt, et al. The effect of mixed wettability on pore-scale flow regimes based on a flooding experiment in ketton limestone. *Geophysical Research Letters*, 46(6):3225–3234, 2019.

[49] Kamaljit Singh, Michael Jung, Martin Brinkmann, and Ralf Seemann. Capillary-dominated fluid displacement in porous media. *Annual Review of Fluid Mechanics*, 2019.

[50] C Chevalier, A Lindner, M Leroux, and E Clément. Morphodynamics during air injection into a confined granular suspension. *Journal of Non-newtonian Fluid Mechanics*, 158(1-3):63–72, 2009.

[51] ITASCA. *PFC2D, v3.1 – Theory and Background.* Itasca Consulting Group, Inc., Minneapolis, MN, 2004.

[52] Mario Scheel, Ralf Seemann, Martin Brinkmann, Marco Di Michiel, Adrian Sheppard, Boris Breidenbach, and Stephan Herminghaus. Morphological clues to wet granular pile stability. *Nature Materials*, 7(3):189, 2008.

[53] SH Ebrahimnazhad Rahbari, J Vollmer, S Herminghaus, and M Brinkmann. Fluidization of wet granulates under shear. *Physical Review E*, 82(6):061305, 2010.

[54] SH Ebrahimnazhad Rahbari, Mahmoud Khadem-Maaref, and SKA Seyed Yaghoubi. Universal features of the jamming phase diagram of wet granular materials. *Physical Review E*, 88(4):042203, 2013.

[55] Zhibing Yang and Ruben Juanes. Two sides of a fault: Grain-scale analysis of pore pressure control on fault slip. *Physical Review E*, 97(2):022906, 2018.

[56] Liv Furuberg, Knut Jørgen Måløy, and Jens Feder. Intermittent behavior in slow drainage. *Physical Review E*, 53(1):966, 1996.

[57] Christopher W MacMinn, Eric R Dufresne, and John S Wettlaufer. Fluid-driven deformation of a soft granular material. *Physical Review X*, 5(1):011020, 2015.

[58] Knut Jørgen Måløy, Liv Furuberg, Jens Feder, and Torstein Jøssang. Dynamics of slow drainage in porous media. *Physical Review Letters*, 68(14):2161, 1992.

[59] Franziska Moebius and Dani Or. Interfacial jumps and pressure bursts during fluid displacement in interacting irregular capillaries. *Journal of Colloid and Interface Science*, 377(1):406–415, 2012.

[60] Andrea J Liu and Sidney R Nagel. *Jamming and rheology: constrained dynamics on microscopic and macroscopic scales*. CRC Press, 2001.

[61] ME Cates, JP Wittmer, J-P Bouchaud, and Ph Claudin. Jamming, force chains, and fragile matter. *Physical Review Letters*, 81(9):1841, 1998.

[62] Ian K Ono, Corey S O'Hern, Douglas J Durian, Stephen A Langer, Andrea J Liu, and Sidney R Nagel. Effective temperatures of a driven system near jamming. *Physical Review Letters*, 89(9):095703, 2002.

[63] Don L Anderson. Through the glass lightly. *Science*, 267(5204):1618–1618, 1995.

[64] Corey S O'Hern, Stephen A Langer, Andrea J Liu, and Sidney R Nagel. Force distributions near jamming and glass transitions. *Physical Review Letters*, 86(1):111, 2001.

[65] TS Majmudar, M Sperl, Stefan Luding, and Robert P Behringer. Jamming transition in granular systems. *Physical Review Letters*, 98(5):058001, 2007.

[66] Silke Henkes and Bulbul Chakraborty. Jamming as a critical phenomenon: A field theory of zero-temperature grain packings. *Physical Review Letters*, 95(19):198002, 2005.

[67] Claus Heussinger and Jean-Louis Barrat. Jamming transition as probed by quasistatic shear flow. *Physical Review Letters*, 102(21):218303, 2009.

[68] Corey S O'Hern, Leonardo E Silbert, Andrea J Liu, and Sidney R Nagel. Jamming at zero temperature and zero applied stress: The epitome of disorder. *Physical Review E*, 68(1):011306, 2003.

[69] Pinaki Chaudhuri, Ludovic Berthier, and Srikanth Sastry. Jamming transitions in amorphous packings of frictionless spheres occur over a continuous range of volume fractions. *Physical Review Letters*, 104(16):165701, 2010.

[70] Corey S O'Hern, Stephen A Langer, Andrea J Liu, and Sidney R Nagel. Random packings of frictionless particles. *Physical Review Letters*, 88(7):075507, 2002.

[71] Leonardo E Silbert, Deniz Ertaş, Gary S Grest, Thomas C Halsey, and Dov Levine. Geometry of frictionless and frictional sphere packings. *Physical Review E*, 65(3):031304, 2002.

[72] Chaoming Song, Ping Wang, and Hernán A Makse. A phase diagram for jammed matter. *Nature*, 453(7195):629, 2008.

[73] Corey S O'Hern, Stephen A Langer, Andrea J Liu, and Sidney R Nagel. Random packings of frictionless particles. *Physical Review Letters*, 88(7):075507, 2002.

[74] Aleksandar Donev, Salvatore Torquato, and Frank H Stillinger. Pair correlation function characteristics of nearly jammed disordered and ordered hard-sphere packings. *Physical Review E*, 71(1):011105, 2005.

[75] SHE Rahbari, J Vollmer, and Hyunggyu Park. Characterizing the nature of the rigidity transition. *Physical Review E*, 98(5):052905, 2018.

[76] Carl P Goodrich, Andrea J Liu, and James P Sethna. Scaling ansatz for the jamming transition. *Proceedings of the National Academy of Sciences*, 113(35):9745–9750, 2016.

[77] Andrea J Liu and Sidney R Nagel. Nonlinear dynamics: Jamming is not just cool any more. *Nature*, 396(6706):21, 1998.

[78] James G Berryman. Random close packing of hard spheres and disks. *Physical Review A*, 27(2):1053, 1983.

[79] Massimo Pica Ciamarra, Raffaele Pastore, Mario Nicodemi, and Antonio Coniglio. Jamming phase diagram for frictional particles. *Physical Review E*, 84(4):041308, 2011.

[80] Ning Xu, Jerzy Blawzdziewicz, and Corey S O'Hern. Random close packing revisited: Ways to pack frictionless disks. *Physical Review E*, 71(6):061306, 2005.

[81] N. Chakrapani, B. Wei, A. Carrillo, P. M. Ajayan, and R. S. Kane. Capillarity-driven assembly of two-dimensional cellular carbon nanotube foams. *Proc. Natl. Acad. Sci. U.S.A.*, 101(12):4009–4012, 2004.

[82] Ebrahim Ghanbari and Hassan Dehghanpour. The fate of fracturing water: A field and simulation study. *Fuel*, 163:282–294, 2016.

[83] A. Skarke, C. Ruppel, M. Kodis, D. Brothers, and E. Lobecker. Widespread methane leakage from the sea floor on the northern US Atlantic margin. *Nature Geoscience*, 7 (9):657, 2014.

[84] A. Parmigiani, S. Faroughi, C. Huber, O. Bachmann, and Y. Su. Bubble accumulation and its role in the evolution of magma reservoirs in the upper crust. *Nature*, 532(7600): 492–495, 2016.

[85] A. L. Handwerger, A. W. Rempel, R. M. Skarbek, J. J. Roering, and G. E. Hilley. Rate-weakening friction characterizes both slow sliding and catastrophic failure of landslides. *Proc. Natl. Acad. Sci. U.S.A.*, 113(37):10281–10286, 2016.

[86] Jane Palmer. Creeping earth could hold secret to deadly landslides. *Nature*, 548(7668): 384–386, 2017.